Check for updates

Advanced Materials

ADVANCED MATERIALS
www.advmat.de

RESEARCH ARTICLE OPEN ACCESS

An Electrically Gated Solid-State Thermal Transistor for Energy-Efficient Thermal Management

Gimin Park[1] | Byoungjin Yoon[1,2] | Yeongdeuk Mun[3] | Kichan Kim[1] | So-Min Song[1,2] | Hyeri Yoo[4,5] | Myoungjin Chung[4,5] | Jeyeon Lee[1,6] | Youngbo Shim[1,7,8] | Sae Bom Chun[1,9] | Sungbin Lee[10] | Jinseong Kim[10] | Woochul Kim[10] | Jeong Min Baik[7,8] | Wonjoon Choi[2] | Ho-Yong Lee[11,12] | Tae Heon Kim[1,13] | Hyoungjeen Jeen[3,14] | Sangtae Kim[15] | Sunghoon Hur[1,7,8,9]

[1]Electronic and Hybrid Materials Research Center, Korea Institute of Science and Technology (KIST), Seoul, Republic of Korea | [2]School of Mechanical Engineering, Korea University, Seoul, Republic of Korea | [3]Department of Physics, Pusan National University, Busan, Republic of Korea | [4]Department of Materials Science and Engineering, Korea University, Seoul, Republic of Korea | [5]Center for Semiconductor Technology, Korea Institute of Science and Technology (KIST), Seoul, Republic of Korea | [6]Department of Micro/Nano Systems, Korea University, Seoul, Republic of Korea | [7]School of Advanced Materials Science and Engineering, Sungkyunkwan University (SKKU), Suwon, Republic of Korea | [8]KIST-SKKU Carbon-Neutral Research Center, Sungkyunkwan University (SKKU), Suwon, Republic of Korea | [9]Division of Energy & Environment Technology, KIST School, Korea National University of Science and Technology (UST), Seoul, Republic of Korea | [10]School of Mechanical Engineering, Yonsei University, Seoul, Republic of Korea | [11]Department of Materials Science and Engineering, Sun Moon University, Asan, Republic of Korea | [12]Ceracomp Co. Ltd., Cheonan, Republic of Korea | [13]Advanced Materials Science and Engineering, KIST School, Korea National University of Science and Technology (UST), Seoul, Republic of Korea | [14]Research Center for Dielectric and Advanced Matter Physics, Pusan National University, Busan, Republic of Korea | [15]Department of Nuclear Engineering, Hanyang University, Seoul, Republic of Korea

Correspondence: Ho-Yong Lee (hlee@sunmoon.ac.kr) | Tae Heon Kim (thkim79@kist.re.kr) | Hyoungjeen Jeen (hjeen@pusan.ac.kr) | Sangtae Kim (sangtae@hanyang.ac.kr) | Sunghoon Hur (hur@kist.re.kr)

Received: 2 July 2026 | **Revised:** 31 October 2026 | **Accepted:** 13 November 2026

Keywords: ferroelectric crystal | thermal conductivity measurement | thermal management system | thermal transport

ABSTRACT

Vapor-compression heating and cooling systems dominate modern thermal management, yet their efficiency and scalability remain constrained by mechanical complexity and refrigerant-based operation. Solid-state approaches offer an attractive alternative, with recent demonstrations showing the potential for highly efficient, compact thermal control. Here we demonstrate an electrically gated solid-state thermal transistor based on bulk single-crystal barium titanate, achieving a switching ratio of 1.6, among the highest reported for bulk ferroelectrics. We further introduce switching efficiency as a figure of merit, reaching ~8.52 $cm^3\ J^{-1}$, more than two orders of magnitude higher than that of the highest-performing reported thermal switch, $PbZrO_3$. Unlike previous thermal switches that operate between two discrete states, this device provides continuously tunable thermal-conductivity states, enabling transistor-like modulation and amplification of heat flow. In situ x-ray diffraction combined with first-principles calculations shows that switching originates from anisotropic phonon transport between ferroelectric domains. Integrated into a proof-of-concept thermal-management system, the device shifts the baseline temperature of a miniature human analog by ~0.6°C at a cycle-averaged power input of 33 μW cm^{-2}, approximately ninefold lower than a vapor-compression heat pump performing the same task. These results establish ferroelectric thermal transistors as a programmable, energy-efficient platform for solid-state thermal management.

Gimin Park, Byoungjin Yoon, and Yeongdeuk Mun contributed equally to this work.

This is an open access article under the terms of the Creative Commons Attribution-NonCommercial-NoDerivs License, which permits use and distribution in any medium, provided the original work is properly cited, the use is non-commercial and no modifications or adaptations are made. All other rights reserved, including rights for text and data mining and training of artificial intelligence technologies or similar technologies.
© 2026 The Author(s). *Advanced Materials* published by Wiley-VCH GmbH

1 | Introduction

Thermodynamic cycle-based systems are among the largest consumers of energy worldwide and major contributors to global carbon emissions [1, 2]. In buildings, space heating and cooling account for nearly half of total energy use [3], with air conditioning and ventilation alone responsible for roughly one-fifth of global building electricity consumption, or about 10% of all electricity use [4]. Reducing the power demand of these systems is therefore central to sustainable energy transitions [5]. While much effort has focused on improving cycle efficiency — through advanced thermal components (e.g., compressors, refrigerants, and heat exchangers) or expanded reservoir temperature ranges — a complementary strategy is to replace or augment the conventional thermal components with solid-state thermal control devices (SSTCDs) that actively manage heat flow directly [6, 7].

Ferroelectric SSTCDs — thermal switches, transistors, diodes, and rectifiers — have emerged as promising candidates in this category as they exhibit electric-field-tunable thermal conductivity k, primarily through domain reorientation and phase transitions [8, 9]. Ferroelectric SSTCDs offer compact, nonmechanical, fast, and quiet operation [7, 10–12]. They act as thermal analogs to electrical circuit components, where an applied electric field E manipulates k [13]. An applied voltage can reversibly toggle a ferroelectric between thermally insulating and conducting states — effectively "switching" heat flow — using minimal energy input. A thermal switch and a thermal transistor are distinguished by how their thermal conductivity is addressed. A thermal switch is addressable between a fixed number of discrete conductivity states, whereas a thermal transistor is addressable continuously across a range by a gate signal, here the electric field. The distinction is functional rather than semantic: a switch selects between a set of heat-flow settings, whereas a transistor sets any value between its limits, and it is on this basis that we describe the device reported here as a transistor.

Among solid-state alternatives to vapor compression, caloric materials have attracted great attention [14, 15]. Electrocaloric systems built from multilayer $Pb(Sc, Ta)O_3$ capacitors have achieved temperature spans of 13 K in regenerative configurations [16]. and above 20 K in double-loop heat pumps, with coefficients of performance reaching approximately half of the Carnot limit [17]. Barocaloric plastic crystals such as neopentylglycol display colossal isothermal entropy changes of several hundred J kg^{-1} K^{-1} near room temperature [18], although the mechanical complexity required to exploit them for solid-state cooling has yet to be overcome [19]. These technologies are the basis of solid-state heat pumps, which transport heat against a temperature gradient. The thermal transistor reported here does not: it modulates the conductive heat flow along a gradient that already exists, so its switching ratio (SR) and a caloric temperature span are not comparable quantities. The two are nonetheless complementary. An efficient caloric cycle requires the caloric device to be alternately coupled to and decoupled from the hot and cold reservoirs, and a solid-state thermal device provides precisely this function without a fluid regenerator [20, 21].

The phenomenon of electrically tunable thermal transport has been demonstrated in a growing number of ferroelectric materials. An early study was based on a $Pb(Zr, Ti)O_3$ (PZT) film, showing a SR of ~1.13 under an applied E [22]. Since then, switching performance has been improved across several materials, including $BaTiO_3$ (BTO) [23–26], $PbTiO_3$ (PTO) [27–29], PZT [30–32], $BiFeO_3$ [33], Poly(vinylidene fluoride) [34], $PbZrO_3$ (PZO) [35, 36], $Pb(Mg, Nb)O_3$-$PbTiO_3$ (PMN-PT) [37–40], and $Hf_{0.5}Zr_{0.5}O_2$ [41]. Notably, first-principles calculations on simple perovskites such as BTO and PTO have indicated strong switching potential arising from their domain-modulation characteristics [29, 42, 43]. The study conducted by Seijas-Bellido et al. was one of the first to predict for monodomain PTO an intrinsic anisotropy $k_\perp / k_\parallel$ exceeding 2 at room temperature, together with a hysteretic $k(E)$ response, but noted that the prediction could not be tested at the time because reported measurements had been made on multidomain samples whose domain populations were unknown [28]. Unlike conventional thermal components in heat pumps or thermoelectric systems, which require substantial continuous energy input during operation, ferroelectric SSTCDs can reversibly modulate heat flow with a brief voltage pulse, then retain the selected thermal state with negligible holding power. This unique characteristic makes them particularly attractive for energy-efficient thermal management [44], especially in building envelopes, where dynamically switchable insulation has been projected to reduce residential energy use by up to 42% [45].

Ferroelectric gating is not the only route to electrically tunable thermal conductivity. Electrochemically driven oxygen-vacancy migration in topotactic oxides achieves considerably larger tuning ranges: reversible cycling of $SrCoO_x$ between brownmillerite, perovskite, and hydrogenated phases by ionic-liquid gating spans nearly a factor of ten in k at room temperature [46, 47], and continuous tuning over a comparable range has been reported for $La_{0.5}Sr_{0.5}CoO_{3-\delta}$ using ion-gel gating [48]. These approaches trade speed and chemical reversibility for range. Because they rely on mass transport rather than lattice displacement, switching proceeds over seconds to hours, requires an electrolyte or elevated temperature, and entails a chemical change of the active layer that ultimately limits endurance. Ferroelectric switching, by contrast, is displacive and involves no mass transport, giving fast and chemically reversible operation at the cost of a smaller accessible range. An intermediate case is oxygen-deficient ferroelectric $HfZrO_2$, in which the polarization acts as an electrically active barrier to oxygen-ion migration; the coupling yields two nonvolatile conductivity states with an on/off ratio of 1.6 at operating voltages below 5 V [41].

In this work, we demonstrate an E-controlled solid-state thermal transistor based on bulk single-crystal BTO that enables active, low-power control of heat transfer. The device exhibits an SR of ~1.6 — one of the highest among reported bulk ferroelectrics. Through in situ x-ray diffraction and first-principles modeling, we show that k is tunable by modulating the orientation of ferroelectric domains, which leads to pronounced anisotropy in phononmediated thermal transport. Unlike previously reported thermal switches, BTO not only toggles between high and low k states but accesses continuous intermediate states as a function of E — enabling true transistor-like control of heat flow. Integrated into a lab-scale thermal system, BTO delivers the same temperature modulation at approximately ninefold lower power than a conventional vapor-compression heat pump when operated on a realistic duty cycle. These results establish ferroelectric-

15214095, 0, Downloaded from https://advanced.onlinelibrary.wiley.com/doi/10.1002/adma.75838 by CochraneChina, Wiley Online Library on [27/11/2026]. See the Terms and Conditions (https://onlinelibrary.wiley.com/terms-and-conditions) on Wiley Online Library for rules of use; OA articles are governed by the applicable Creative Commons License

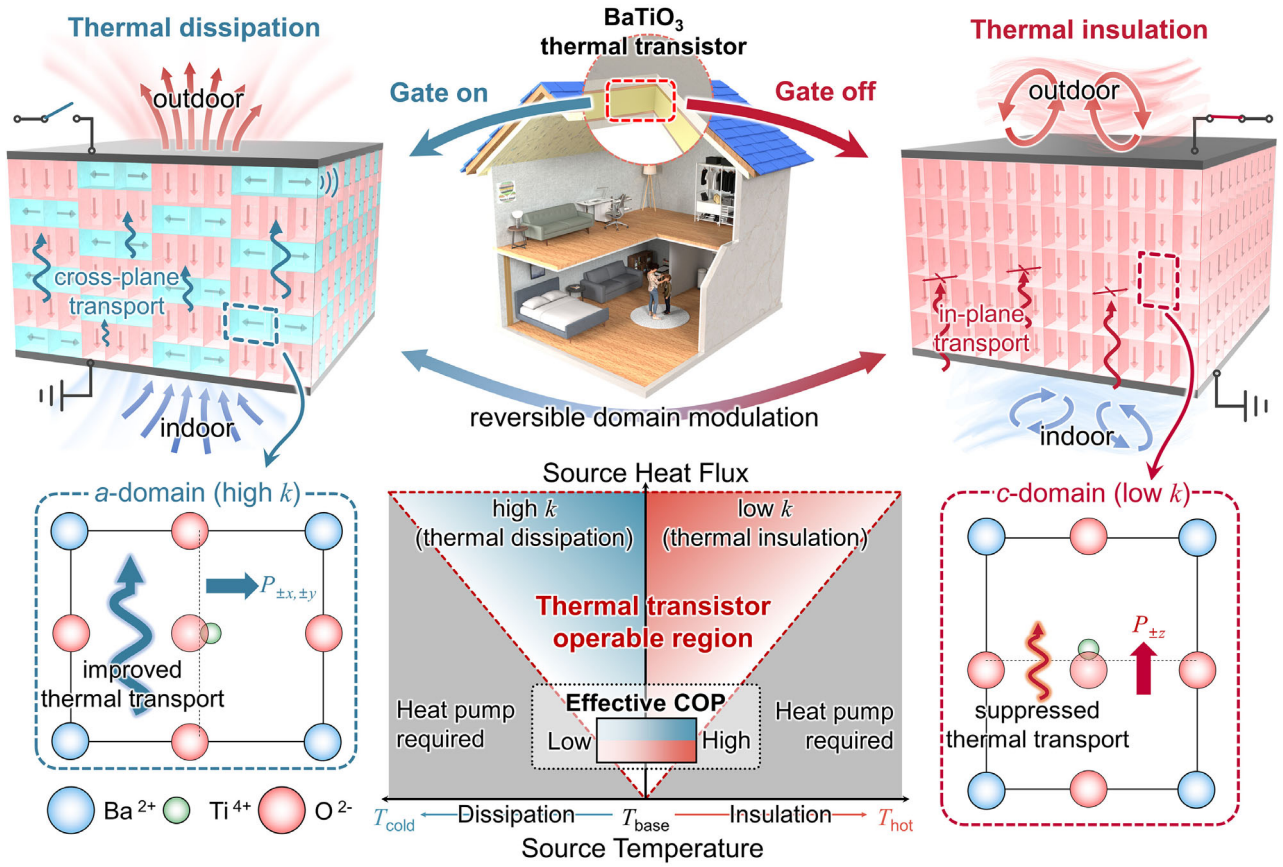


FIGURE 1 | $BaTiO_3$ switching between thermal insulation and dissipation modes for thermal management. The difference in thermal transport between *a*- and *c*-domains determines the transistor-operable range as a function of source temperature and heat flux.

based thermal transistors as compact, programmable platforms for thermal management, with the potential to radically lower the carbon footprint of air conditioning systems.

2 | Results and Discussion

2.1 | Controlling Heat With Ultralow Power Consumption

The BTO thermal transistor serves as an electrically driven active thermal regulator in practical applications such as infrastructure walls by switching between two operational modes: thermal insulation (low k) and dissipation (high k), as illustrated in Figure 1. Barium titanate adopts a tetragonal crystal structure at room temperature, exhibiting anisotropic thermal transport — specifically, a difference in k along the [001] and [100]/[010] directions. This behavior extends to its ferroelectric domain configurations: *a*-domains, polarized in-plane (±[100] or ±[010]), and *c*-domains, polarized out-of-plane (±[001]), as illustrated in Figure 1. While crystallographically identical, these domains differ in their phonon transport along the [001] direction due to anisotropic lattice dynamics. Exploiting this feature, we demonstrate that k of BTO can be modulated by applying E, enabling its function as an electrically tunable thermal transistor.

The function of the BTO thermal transistor becomes meaningful only in the presence of a finite temperature gradient between a heat source and a sink (Figure 1); unlike heat pumps, it cannot actively transfer heat against a thermal gradient. Rather, it modulates the conductive heat flux that naturally arises from an existing temperature difference. In scenarios where the source generates a substantial amount of heat, BTO can effectively switch between dissipation and insulation without requiring active refrigeration or heating, as illustrated in Figure 1. Because the achievable modulation in k is finite, the extent of temperature control is also limited. Nevertheless, because BTO requires meaningful energy only during polarization switching and not to maintain a given state, its effective coefficient of performance (COP) under steady operation can substantially exceed that of conventional heat pumps. Moreover, the effectiveness of thermal regulation increases with source heat flux, as a larger intrinsic temperature gradient enhances the impact of k modulation.

To define the operational window of the device, we first evaluated its heat-control performance by positioning the BTO transistor between a controlled heat source and sink (Figure S1). In the on-demand temperature-control mode, the heat source generated a constant heat flux of 300 mW cm^{-2}. The modulation of k in BTO enabled control of the heater temperature by ~0.9 K. The attainable temperature modulation is expected to increase with larger source heat fluxes, because the conductive heat flux scales as $q \propto k \times \Delta T$. In the on-demand thermal-management mode, the heat-source temperature was maintained at 30°C. The modulation of k enabled reversible switching between insulation and dissipation states and modulated heat flux by ~15%. Together, these results

15214095, 0, Downloaded from https://advanced.onlinelibrary.wiley.com/doi/10.1002/adma.75838 by CochraneChina, Wiley Online Library on [27/11/2026]. See the Terms and Conditions (https://onlinelibrary.wiley.com/terms-and-conditions) on Wiley Online Library for rules of use; OA articles are governed by the applicable Creative Commons License

demonstrate stable, repeatable, and practically relevant electrical gating of heat flow in bulk ferroelectric BTO.

The temperature modulation achieved by the device is not an intrinsic figure of merit but the product of the switchable thermal resistance R''_{sw} and the heat flux q'' through the device, $\delta T = q''l(\frac{1}{k_{low}} - \frac{1}{k_{high}}) = q''R''_{sw} = 1.38 \times 10^{-4}$ m^2 K W^{-1} for the 1 mm crystal used here. Ideally, the device modulates a fixed fraction $1 - k_{low}/k_{high} = 37\%$ of whatever temperature drop it sustains. The ~0.9 K measured in Figure S1 corresponds to a flux of 6.75×10^3 W m^{-2} through the crystal and is reproduced by this expression to within 3%. At the higher fluxes of battery packs and power electronics, on the order of 1 W cm^{-2}, the same device would modulate ~1.4 K, rising to ~14 K at 10 W cm^{-2} (Figure S2). Where the source temperature is instead held fixed, as in a building envelope, the relevant quantity is the modulation of heat flux rather than of temperature; the ~15% measured here is limited by the series resistance of the assembly rather than by the material, and approaches 37% as that resistance is reduced. The device is accordingly suited to applications requiring a switchable thermal insulator — battery thermal management, spacecraft variable-conductance links, dynamically insulating building elements, and the coupling of caloric devices to their reservoirs — rather than for use as a low-resistance heat path.

To assess the performance of the thermal transistor in a more realistic scenario, we constructed a miniature thermal system comprising a scaled-down house and a human analog positioned atop the BTO transistor (Figure 2a). The human analog contains an embedded temperature sensor and heater programmed to simulate sinusoidal heat generation. In insulation mode (E = 10 kV cm^{-1}), the person's initial baseline temperature drifts below the comfort range (36°C–37°C), signaling a need for heat conservation. When E is applied along [001], ferroelectric domains reorient — rotating by 90° or 180° — and transform a-domains into c-domains. This domain alignment suppresses heat transfer, raising the baseline temperature by ~0.6°C and bringing it within the target comfort range. Notably, the electric power density required to induce this switching is minimal — just 8.8 μW cm^{-2} — which was measured at E = 10 kV cm^{-1} (Figure 2b and Figure S3). Conversely, in dissipation mode (near coercive field E_c = −1 kV cm^{-1}), the system cools the overheated analog by improving heat transfer through the BTO transistor, again restoring thermal comfort. Here, the required power density is 57.5 μW cm^{-2} due to larger polarization switching currents, as shown in Figure S3. Infrared snapshots extracted from Movies S1 and S2 clearly illustrate the baseline temperature shift in both modes and show that the switching performance of BTO functions effectively as a thermal transistor.

For comparison, we evaluated the energy efficiency of a commercially available Peltier device in the same thermal setup. Operating under bipolar current, the Peltier device toggles between heating and cooling, shifting the baseline temperature of the miniature person by ±0.6°C (Figure S4). As is well known, Peltier devices perform extremely inefficiently, with a COP of less than 1 (0.6 is assumed in this study). The device used in this study draws a power density of up to 1.5 mW cm^{-2} for thermally managing the heat-generating human analog. For the same thermal setup, a vapor-compression-based heat pump with a typical COP of 3 is expected to draw power densities of up to ~300 μW cm^{-2}. Accordingly, Figure 2c presents the performance of the BTO transistor benchmarked against a vapor-compression-based heat pump and a Peltier device. Over a complete operating cycle, the input comprises the energy of polarization reversal and the power required to hold the selected state. For a device switched twice daily and spending equal time in the insulating and dissipating states, the time-averaged input is 33 μW cm^{-2}, of which the switching contribution is 0.1%, and the device draws approximately ninefold less power than a vapor-compression heat pump performing the same thermal task (Figure S5).

Although SR is central to heat-flow modulation, practical deployment also requires consideration of device energy efficiency. We therefore introduce a new figure of merit, the switching efficiency ε, defined as:

$$\varepsilon = \frac{(SR-1)}{U} = \left(\frac{k_{high} - k_{low}}{k_{low}} - 1\right) \Big/ \int_{P_f}^{P_i} E(P)dP.$$

Here, ε is defined from an initial polarization state P_i to a final state P_f. U is the input energy density (J m^{-3}), and P is the polarization. The input energy density is the work done by the field on the polarization along the switching path, $U = \int EdP$ from the initial to the final polarization (Text S1). Figure 2d compares ε of BTO with those of previously reported ferroelectric thermal switches. Among bulk ferroelectrics reported to date, BTO exhibits one of the highest switching efficiencies, owing to its large SR and low operating E. Other bulk materials require comparable input energy but exhibit smaller SR, whereas thin films, despite their high SR, operate at electric fields one to two orders of magnitude larger and therefore require a substantially higher input energy density, yielding lower ε.

We note that thin films operate at lower voltages owing to their small thickness; we adopt electric field as the comparison metric because ε is normalized by the input energy density, an intrinsic material property, whereas voltage scales with thickness. This distinction is consequential for SSTCDs, in which the switchable thermal resistance $R''_{sw} = l(\frac{1}{k_{low}} - \frac{1}{k_{high}})$ scales with thickness: sub-micrometer films present thermal conductances so high that they act as "thermal shorts" in a macroscopic assembly, and matching the switchable resistance of a bulk device would require comparable thickness and hence far higher voltage. Thin-film and bulk devices therefore occupy complementary regimes — the former suited to on-chip hot spot control, the latter to macroscopic heat management (Text S2 and Figure S6).

The device is thermally rather than electrically limited: the switching time constant τ_s = 27–38 ms, whereas the thermal time constant ($\tau_{th} = l^2/\alpha$) of the 1 mm device is 0.97 s in the insulating state and 0.61 s in the dissipating state (Figure S7 and Table S1), where α is the thermal diffusivity. The source temperature must therefore vary on a timescale longer than approximately 1 s for the device to track it, and faster operation requires a thinner device at a proportional cost in switchable thermal resistance.

The device modulates conductive heat flow along an existing temperature difference and cannot transport heat against one; it is

15214095, 0, Downloaded from https://advanced.onlinelibrary.wiley.com/doi/10.1002/adma.75838 by CochraneChina, Wiley Online Library on [27/11/2026]. See the Terms and Conditions (https://onlinelibrary.wiley.com/terms-and-conditions) on Wiley Online Library for rules of use; OA articles are governed by the applicable Creative Commons License

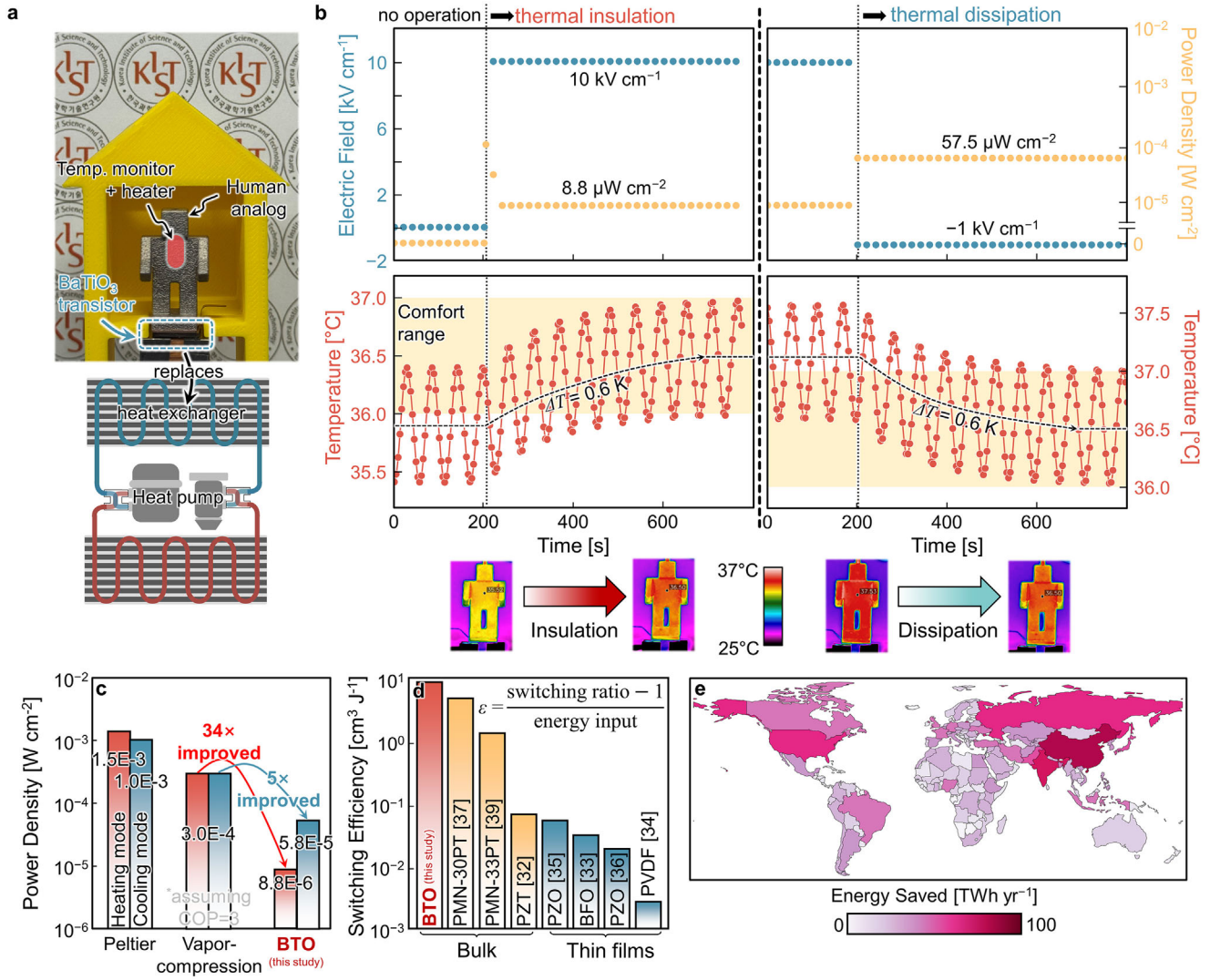


FIGURE 2 | Demonstration of thermal regulation using a miniature house model. (a) Experimental setup for evaluating the performance of BTO. (b) Thermal management of the human analog as a function of the applied electric field. (c) Power density of BTO compared with a conventional heat pump and a Peltier cooler. (d) Comparison of switching efficiency among representative ferroelectric thermal switches and transistors. (e) Estimated country-level electricity savings from operating the transistor in series with a conventional heat pump at a required temperature modulation of 20 K.

therefore not a substitute for a heat pump, and we do not estimate the energy that would be saved by replacing heat pumps with it. What the device can do is reduce the temperature lift a heat pump must supply. Operating in series with a conventional system, the transistor delivers the first $\Delta T_{BTO} = 0.6$ K of the required modulation at a time-averaged input $P_{BTO} = 33\ \mu W\ cm^{-2}$, against the $P_{HP}\ \Delta T_{BTO} = 300\ \mu W\ cm^{-2}$ a heat pump would draw for the same increment, where $P_{HP} = 500\ \mu W\ cm^{-2}\ K^{-1}$. The combination therefore saves $\Delta P = P_{HP}\ \Delta T_{BTO} - P_{BTO} = 267\ \mu W\ cm^{-2}$ irrespective of the total modulation required, a fraction $\Delta P/(P_{HP}\ \Delta T)$ of the heat-pump input, which for a representative required modulation of $\Delta T = 20$ K is 2.7%. Applying this fraction to the climate- and population-weighted demand model of Text S3 gives the country-level savings mapped in Figure 2e, with the heating and cooling breakdown in Figure S8. Against global heating- and cooling-related electricity consumption of 19,000 TWh annually [4, 49], this corresponds to approximately 500 TWh yr^{-1}, concentrated in populous regions with extreme seasonal variation. The saving scales inversely with the required modulation (Figure S9), and is realized only during periods in which the ambient gradient runs in the direction the application requires.

2.2 | In Situ Measurement of Tunable Thermal Transport

To quantify the E-dependent k of BTO, we developed a custom property measurement system (PMS) as presented in Figure 3a and Figure S10. The system enables simultaneous measurement of E-dependent k, P, electric current, and contact pressure induced by the inverse-piezoelectric-effect. The experiments were conducted under vacuum to minimize convective heat loss.

Determining k requires solving the thermal resistance network of the PMS (Figure 3a). Accurate extraction of k also requires determining the thermal contact resistance R_{tc} at the top and bottom surfaces of the BTO and the parasitic heat loss coefficient h_{loss} associated with conduction through wires and radiative loss

15214095, 0, Downloaded from https://advanced.onlinelibrary.wiley.com/doi/10.1002/adma.75838 by CochraneChina, Wiley Online Library on [27/11/2026]. See the Terms and Conditions (https://onlinelibrary.wiley.com/terms-and-conditions) on Wiley Online Library for rules of use; OA articles are governed by the applicable Creative Commons License

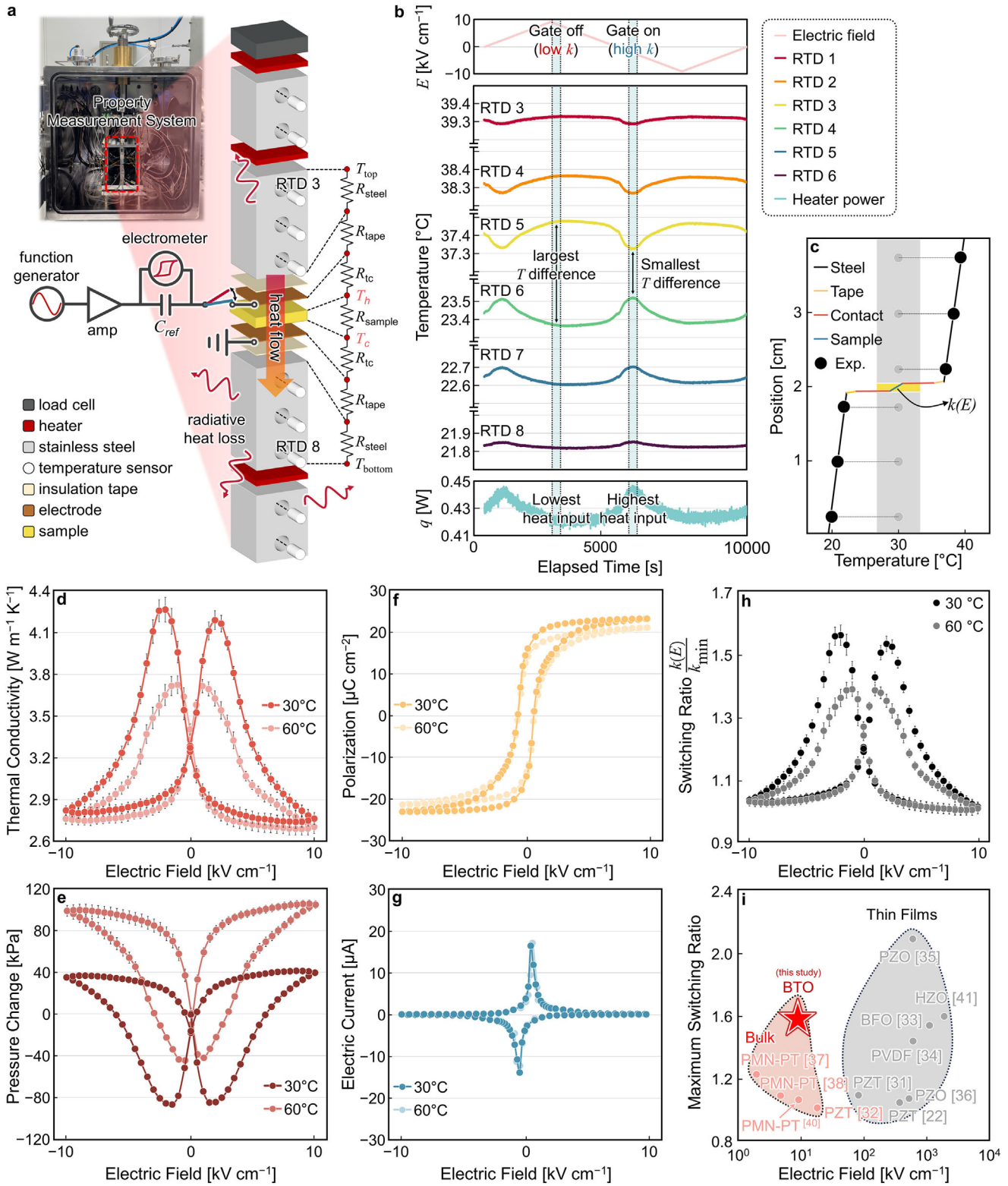


FIGURE 3 | Electric-field-dependent thermal and electrical properties measured using a custom property measurement system. (a) Experimental platform for simultaneous measurement of thermal conductivity k, polarization, electric current, and field-induced contact pressure. The schematic includes the thermal resistance model used to extract k. (b) Representative temperature and heater power responses under a sweeping electric field. (c) Determination of thermal conductivity from spatial temperature profiles. (d) Electric-field-dependent k; (e) field-induced contact pressure change; (f) polarization, (g) electric current, and (h) switching ratio SR. (i) Comparison of the maximum SR of BTO with other bulk and thin-film ferroelectric devices. Error bars denote the standard deviation over five complete field cycles.

15214095, 0, Downloaded from https://advanced.onlinelibrary.wiley.com/doi/10.1002/adma.75838 by CochraneChina, Wiley Online Library on [27/11/2026]. See the Terms and Conditions (https://onlinelibrary.wiley.com/terms-and-conditions) on Wiley Online Library for rules of use; OA articles are governed by the applicable Creative Commons License

from the stainless-steel block surfaces. The full derivation for determining k is given in Text S4.

We determined h_{loss} independently by imposing symmetric boundary conditions ($T_{bottom} = T_{top}$), under which the PMS develops a temperature profile symmetric about the center of the structure. Because this profile is independent of the thermal conductivity of BTO, fitting the measured profile directly yields h_{loss}, which was found to be ~8.6 W m^{-2} K^{-1} (Figure S11a and Text S5). We then determined R_{tc} by varying the contact pressure applied to BTO and measuring the corresponding pressure-dependent temperature profiles. Since k of BTO remains unchanged with contact pressure, the observed profile changes can be attributed solely to variations in R_{tc}. To enable this analysis, the specific heat c_p, α, and k of a [001]-poled BTO crystal were first measured using commercial instruments (Figure S12 and Text S5). These values set the absolute scale of the subsequent field-dependent measurements. From the pressure-dependent PMS temperature profiles, we then extracted the pressure-dependent contact resistance $R_{tc}(P)$, as shown in Figure S11b. With h_{loss} and $R_{tc}(P)$ established, we subsequently determined the field-dependent k (i.e., $k(E)$).

Figure 3b shows the transient temperature and heater-power responses at a sample temperature of ~30°C during E cycling from −10 to 10 kV cm^{-1}, using 0.25 kV cm^{-1} steps held for 60 s. One full cycle takes approximately 3 h. The evolving temperature and heater-power signals indicate continuous changes in the thermal resistance of the system with electric field, consistent with E-dependent k. The largest temperature gradient and lowest heater power are observed at the maximum electric field (E_{max}), corresponding to the minimum k, whereas the smallest temperature gradient and highest heater power occur near the coercive field E_c, where k reaches its maximum. Temperature profiles acquired at each E step were fitted to a theoretical model (Figure 3c and Text S4) to extract the field-dependent k. The resulting thermal, mechanical, and electrical responses are summarized in Figure 3d–g. Consistent with Figure 3b, k reaches a maximum of ~4.3 W m^{-1} K^{-1} near $\pm E_c$ and a minimum of ~2.7 W m^{-1} K^{-1} near $\pm E_{max}$. This behavior reflects ferroelectric domain reorientation: a c-domain-dominant state at $\pm E_{max}$ gives the lowest k, whereas the mixed a- and c-domain state near $\pm E_c$ gives the highest k. The resulting $k(E)$ response is hysteretic, following different values on the ascending and descending branches, in qualitative agreement with the behavior predicted for monodomain $PbTiO_3$ [28]. The sample also exhibits E-induced strain through the inverse piezoelectric effect, which alters the thermal contact resistance between the sample and electrodes. Because $R_{tc}(P)$ has been determined from a previous set of experiments (Figure S11b), variations in contact resistance are properly accounted for in the analysis. The uncertainties in both calibrations are propagated, together with the repeatability of the measurement, in Text S6.

Device stability was evaluated over five consecutive thermal cycles (~17 h total; Figure S13). The change in k between cycles remained below 2%, indicating highly reproducible switching with negligible degradation. To examine possible material changes induced by cycling, x-ray diffraction (XRD) patterns were obtained before and after the durability test. As shown in Figure S14, no secondary peaks emerged after cycling, indicating minimal structural degradation. Additionally, endurance under electrical cycling was tested separately. The thermal conductivity of the device was measured over 12 thermal cycles before and again after 10^3, 10^4, and 10^5 cycles at ±10 kV cm^{-1}, for a total of 48 thermal cycles (Figure S15). Both conductivity states changed by about 2%, comparable to the scatter between successive cycles, while the SR changed by less than 1%. A recent study by Zhang et al. also reported E-dependent k (~35%) in unpoled Barium Titanate single crystals, differing from our results due to several factors [26]. First, Zhang et al. measured unpoled crystals including initial irreversible poling, whereas our data reflect stable, reversible switching after initial stabilization (Supporting Information, Methods). Second, the main source of the difference in magnitude, is that Zhang et al. measured in-plane k, with heat flowing perpendicular to E, whereas we measure cross-plane k, with heat flowing along E. For equal populations of the two a-domain variants, the same domain switching changes k half as much in-plane as cross-plane. Finally, the crystals were grown by different routes, by top-seeded solution growth in their study and by solid-state crystal growth here (Supporting Information, Methods), resulting in distinct defect dipoles and behaviors that are not directly comparable.

The SR as a function of E is shown in Figure 3 h and reveals true transistor-like behavior, demonstrating both amplification and switching of thermal conductivity. In addition to this behavior, an SR of ~1.6 ± 0.07 is obtained at 30°C, decreasing slightly to ~1.4 at 60°C. At 60°C, stronger thermal vibrations of the atoms reduce the fraction of switchable domains and weaken the macroscopic polarization response [50, 51], which ultimately reduces SR by ~20% relative to that at 30°C. Among bulk ferroelectric materials, BTO exhibits the highest value (Figure 3i); although the antiferroelectric PZO film outperforms bulk BTO, it requires substantially higher electric fields [35].

2.3 | Mechanism for Tunable Thermal Transport

The origin of tunable thermal transport in ferroelectrics remains debated. Proposed mechanisms include primitive unit cell modulation, domain-wall scattering, and field-induced phase transitions, including order-disorder and displacive transitions [9, 38, 52–54]. No universal framework has yet emerged. For BTO, however, the dominant factor is expected to be the intrinsic anisotropy in phonon transport between a- and c-domains, which enables large tunability of k and underpins such a high SR. Direct evidence for this anisotropy has been provided by Féger et al., who resolved the thermal conductivity of individual a- and c-domains of $BaTiO_3$ by scanning thermal microscopy and reported a thermal conductivity ratio k_a/k_c of 1.6 ± 0.3 between them [25]. That measurement establishes the microscopic premise on which the present device rests. What the domain-resolved measurement does not determine is how much of that contrast the device as a whole can deliver. The thermal conductivity ratio is a property of the material; the SR delivered by a device is set by the domain populations an applied field can actually produce. Under a field applied along [001], the crystal never reaches an a-domain-dominant state, so the two quantities differ and the second cannot be inferred from the first. We therefore determine the domain populations directly under field by in situ x-ray diffraction, and relate them to the volume-averaged conductivity that governs heat flow through the device.

15214095, 0, Downloaded from https://advanced.onlinelibrary.wiley.com/doi/10.1002/adma.75838 by CochraneChina, Wiley Online Library on [27/11/2026]. See the Terms and Conditions (https://onlinelibrary.wiley.com/terms-and-conditions) on Wiley Online Library for rules of use; OA articles are governed by the applicable Creative Commons License

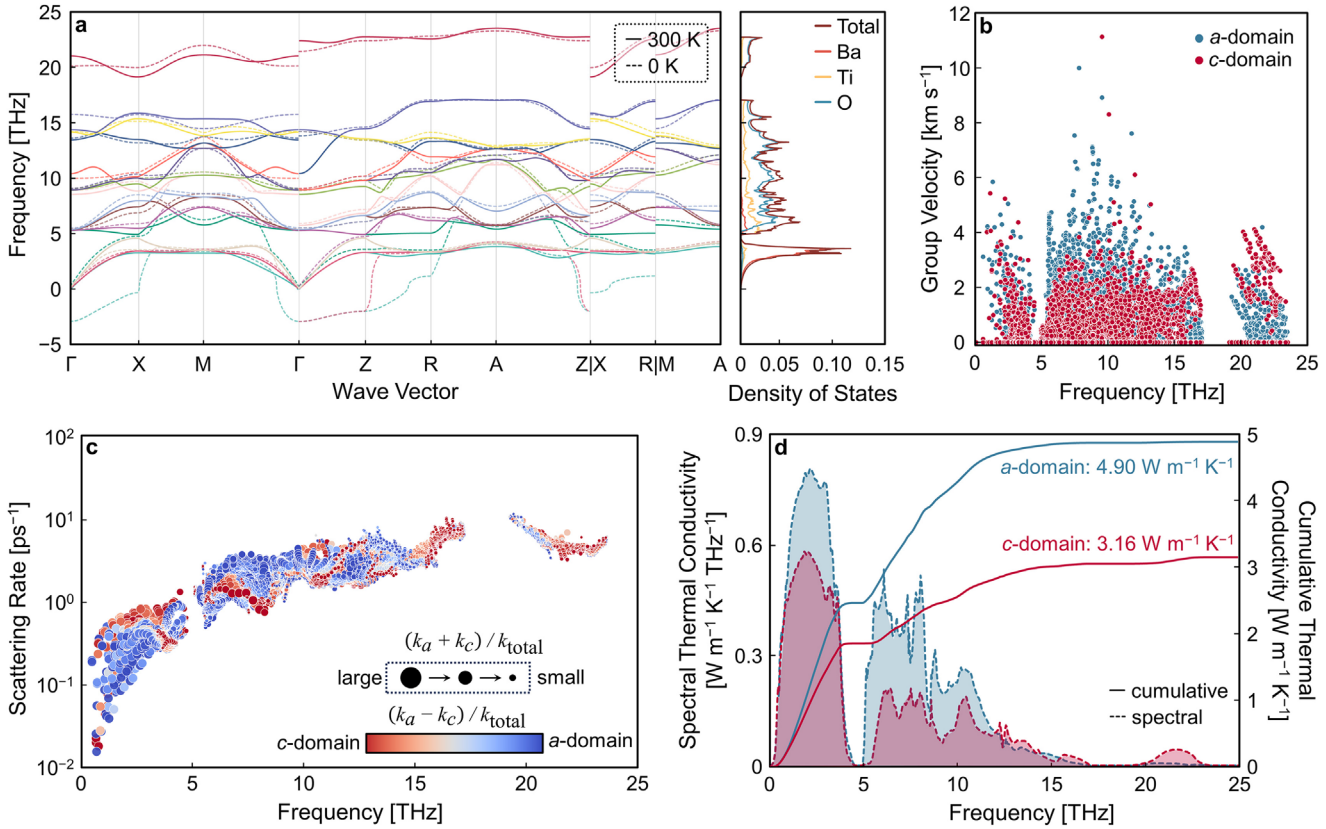


FIGURE 4 | First-principles analysis of phonon transport in *a*- and *c*-domain BTO. (a) Harmonic (0 K) and anharmonic (300 K) phonon dispersion relations of tetragonal BTO. (b) Phonon group velocity for *a*- and *c*-domains. (c) Phonon scattering rates. Symbol size represents the modal contribution to total thermal conductivity k, and color indicates the dominant domain contribution. (d) Spectral and cumulative k of *a*- and *c*-domains, showing strong anisotropy in phonon transport.

We therefore performed first-principles calculations to quantify domain-resolved phonon transport (Text S7). Tetragonal BTO exhibits unstable soft polar modes in conventional density functional theory (DFT), leading to imaginary phonon frequencies at 0 K [55–57]. These imaginary modes result in underestimated and physically unreliable thermal conductivity values, as they neglect relevant phonon contributions and impose reduced group velocities (Figure S16). To obtain physically meaningful finite-temperature phonon properties, we employed self-consistent phonon (SCPH) calculations using the ALAMODE package (Text S7). Figure 4a compares harmonic (0 K) and anharmonic (300 K) phonon dispersions, demonstrating removal of imaginary modes at a finite temperature. The high-symmetry points of the crystal are depicted in Figure S17. Lattice thermal conductivity can be estimated within the relaxation-time approximation, in which k is expressed as:

$$k(T) = \frac{1}{VN_\lambda} \sum_\lambda c_{p,\lambda} v_\lambda^2 \tau_\lambda$$

where V is the unit cell volume, N is the number of unit cells, c_p is the mode-specific heat capacity, v is the group velocity, and τ is the relaxation time. Clearly, domain-resolved c_p, v, and τ must be determined to calculate the domain-specific k of BTO.

Accordingly, the domain-specific phonon group velocities are plotted in Figure 4b. While the low- and high-frequency phonon branches are similar for both *a*- and *c*-domains, the group velocities of mid-frequency phonons are systematically higher in the *a*-domain. The unweighted average group velocity is 0.94 km s^{-1} for the *a*-domain, compared with 0.84 km s^{-1} for the *c*-domain, corresponding to an approximately 12% difference. The phonon-phonon scattering rates ($1/\tau$) are presented in Figure 4c. Because phonon modes cannot be uniquely attributed to a specific ferroelectric domain, we instead specify the domain for which each mode makes a stronger contribution to k; the marker size represents the modal contribution to cumulative k, and color denotes the domain to which the mode contributes more significantly. Low-frequency acoustic phonons — primarily contributing to the *a*-domain — exhibit lower scattering rates, whereas modes associated more strongly with the *c*-domain display higher scattering rates. This difference originates from a reduced three-phonon scattering phase space, implying fewer momentum- and energy-conserving scattering channels for heat-carrying phonons. Because the scattering phase space itself cannot be decomposed by domain, only the domain-independent phase-space distributions are shown in Figure S18.

The combined differences in group velocity and scattering rate give rise to significant variations in k between *a*- and *c*-domains. Figure 4d shows calculated k values of 4.89 W m^{-1} K^{-1} for the *a*-domain and 3.16 W m^{-1} K^{-1} for the *c*-domain — these values correspond to k_a/k_c = 1.55. The calculation describes a perfect, defect-free monodomain crystal with only three-phonon

15214095, 0, Downloaded from https://advanced.onlinelibrary.wiley.com/doi/10.1002/adma.75838 by CochraneChina, Wiley Online Library on [27/11/2026]. See the Terms and Conditions (https://onlinelibrary.wiley.com/terms-and-conditions) on Wiley Online Library for rules of use; OA articles are governed by the applicable Creative Commons License

scattering, and reported single-domain conductivities of tetragonal BTO vary considerably: 4.5/3.7 [25], 6.2/4.2 [24], and 6.2/3.3 W m^{-1} K^{-1} [26] among calculations, and 5.5/4.0 [52] and 3.9/2.6 W m^{-1} K^{-1} [25] among measurements. The calculation therefore establishes the origin, sign, and spectral composition of the anisotropy robustly, while the absolute single-domain values carry an uncertainty comparable to the spread among these reports — a distinction that becomes relevant when the model is compared quantitatively with the measured $k(E)$ below.

Mesh convergence tests (Figure S19a) confirm numerical stability, with variations below 0.5%. Across nearly the entire acoustic frequency range, the spectral k of the a-domain exceeds that of the c-domain due to lower scattering rates, as seen in Figure 4c. This is true for mid-range optical phonons as well (5–13 THz), as the group velocities for the a-domain are much higher, whereas the scattering rates differ little between domains. In contrast, near 22 THz, the group velocities are higher for the c-domain; however, these high-frequency optical phonons exhibit large scattering rates, resulting in a small contribution to the cumulative k. As presented in Figure S19b, over the temperature range where BTO remains tetragonal, the k ratio of a- to c-domain changes only marginally (1.56 to 1.52), indicating robust anisotropy. The effect of lattice strain induced by the inverse piezoelectric response is also expected to be negligible, as the dominant contribution to the observed difference in k of a- and c-domains arises from intrinsic crystallographic anisotropy [26].

Having established intrinsically different thermal transport in a- and c-domains, we next determine how domain populations contribute to k. Figure 5a presents the experimental schematic of in situ XRD measurements under an applied electric field along [001], and Figure 5b shows the resultant domain reorientation. In its virgin state, BTO contains mixed a- and c-domains (~2:1 ratio). Applying E drives the crystal toward a c-domain-dominant state; removing the field partially restores a-domains. While the initial poling is irreversible, subsequent switching between E_{max} and E_c states is reversible.

Figure 5c shows diffraction contours during field cycling from $+E_{max}$ to $-E_{max}$ and back. In situ XRD patterns around the BTO (002) (c-domain) and (200) (a-domain) reflections were collected over the 2θ range of 44°–46°. The (002) and (200) peak intensities vary systematically with field. Specifically, as shown in Figure 5d, at $\pm E_{max}$, the (002) peak dominates, indicating near-complete c-domain alignment. As the electric field is swept from $+E_{max}$ to $-E_{max}$ and back, the (200) peak intensity increases near $-E_c$ and $+E_c$, respectively, reflecting the re-emergence of a-domains. Diffraction peaks corresponding to a- and c-domain reflections were fitted using a split pseudo-Voigt profile to accurately account for peak asymmetry and extract integrated intensities (Figure S20) [58], which were converted to volume fractions (Figure 5e) [59]. At $\pm E_{max}$, the a-domain fraction approaches zero; near $\pm E_c$, the a-to-c domain ratio approaches ~0.45:0.55. If BTO is treated as a composite medium with a- and c-domains randomly distributed, the effective k can therefore be modeled as:

$$k = \upsilon_a k_a + \upsilon_c k_c$$

where υ is the domain volume fraction, and the subscripts indicate the domain. Using the calculated domain k (Figure 4d) together with the measured domain fractions (Figure 5e), we predict that k reaches a minimum near $\pm E_{max}$ and a maximum near $\pm E_c$, consistent with the experimental trend, as shown in Figure 5f. The predicted amplitude is smaller than the measured one, for the reason set out in Texts S7 and S8 (Figure S21). The continuum of states is addressable in the sense defined by a thermal transistor: the applied field sets υ_a and υ_c, and k follows from domain mixing, so every value between 2.7 and 4.3 W m^{-1} K^{-1} is accessible, and each is held for as long as the field is applied (Figure S22).

Domain-wall scattering, proposed as a dominant tunable-transport mechanism in ferroelectric thermal switches, is expected to be negligible under the present room-temperature bulk single-crystal conditions [38, 54]. Our first-principles calculations show that the dominant heat-carrying phonons in BTO at 300 K have short mean free paths (MFPs), with most contributions arising from modes in the 1–50 nm range [24]. In contrast, domain wall spacings in bulk BTO single crystals are well established in the range of 20–100 μm or larger depending on the poling state, as directly visualized by polarized optical microscopy in previous studies [60]. The ratio of domain wall spacing to phonon MFP therefore exceeds two orders of magnitude across all experimental conditions in this study, ensuring that phonon-phonon scattering overwhelmingly dominates. This conclusion is further supported by the field dependence of k observed in this work: domain wall density is likely to be highest in the mixed a- and c-domain state near $\pm E_c$, yet k reaches its maximum at this field — the opposite of the trend a domain wall scattering mechanism would produce.

Finally, we consider what bounds the switching performance (Figure 5 g). Because the field is applied along [001], it can drive the crystal toward a c-domain-dominant state but not toward an a-domain-dominant one, and the accessible domain populations are bounded accordingly: in situ diffraction places υ_a between 0.075 at $\pm E_{max}$ and 0.454 near $\pm E_c$ ("Achievable"). This is what converts a material property into a device specification — the thermal conductivity ratio k_a/k_c belongs to the material, whereas the SR a device delivers is fixed by the domain populations the field can reach, and over this range the two-component mixing relation returns a SR well below k_a/k_c. Greater modulation would require higher a-domain fractions than a [001] field can produce ("Not demonstrated"), which field orientations along [100] or [010] could in principle access. Such multi-axis polarization control suggests a pathway toward larger SRs in BTO-based thermal transistors and in other ferroelectrics with anisotropic phonon transport.

3 | Concluding Remarks

We demonstrate that bulk single-crystal BTO can function as a solid-state thermal transistor capable of actively modulating the amount of heat transferred from a heat source to a sink. Owing to its large SR and ultralow power consumption, its effective COP is approximately ninefold higher than that of a conventional vapor-compression-based heat pump when operated on a realistic cycle. The device reversibly modulates the baseline temperature of a miniature human analog by ~0.6°C, comparable to the control range achieved by a commercial Peltier device. Among bulk

15214095, 0, Downloaded from https://advanced.onlinelibrary.wiley.com/doi/10.1002/adma.75838 by CochraneChina, Wiley Online Library on [27/11/2026]. See the Terms and Conditions (https://onlinelibrary.wiley.com/terms-and-conditions) on Wiley Online Library for rules of use; OA articles are governed by the applicable Creative Commons License

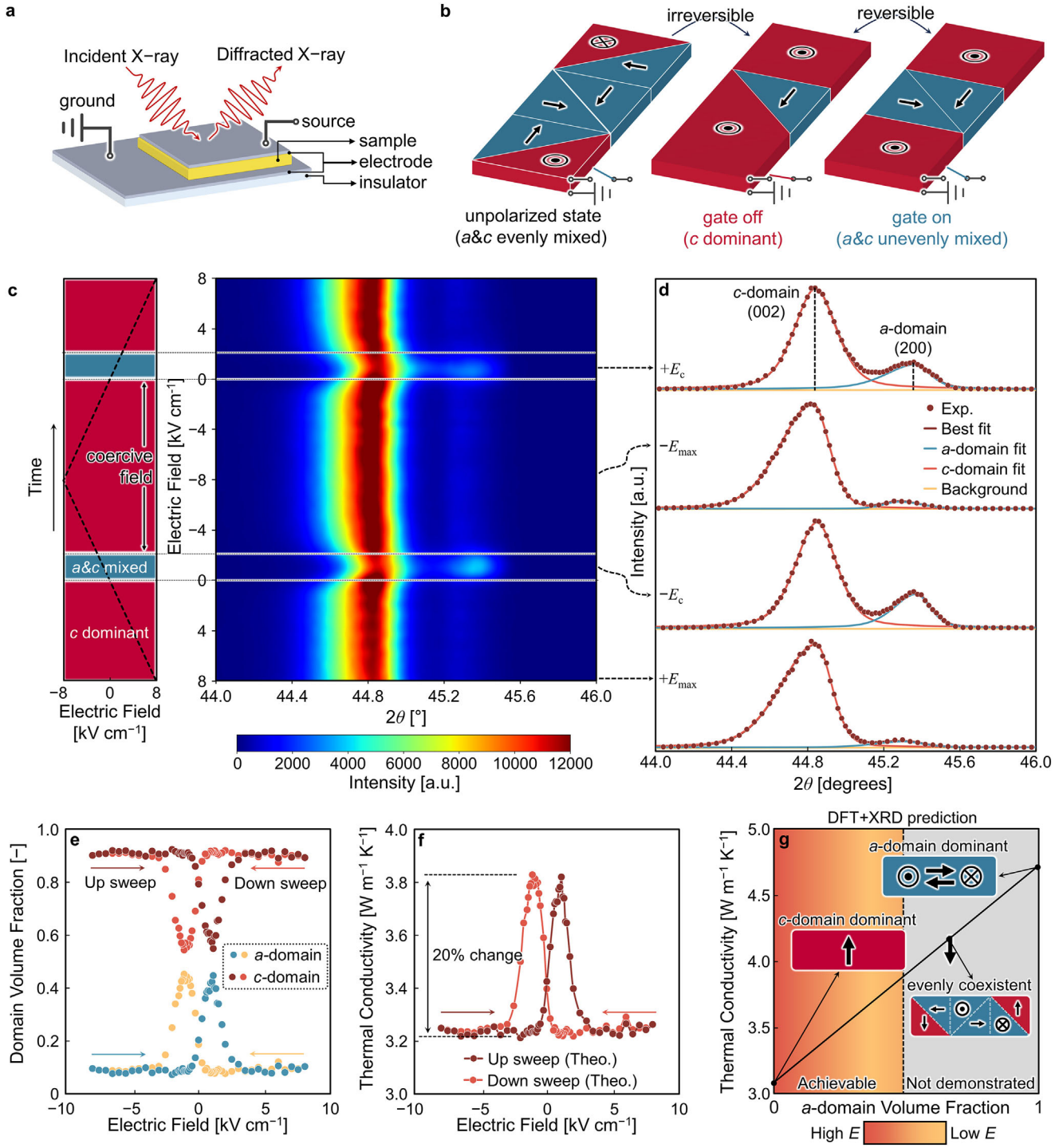


FIGURE 5 | Electric-field-dependent domain evolution and predicted effective thermal conductivity k. (a) Schematic of in situ electric-field-dependent x-ray diffraction measurement. (b) Domain reconfiguration under applied electric field E. (c) Contour map of diffraction intensity near (002) and (200) reflections. (d) Evolution of (002) and (200) intensities with E; curves are fitted using split pseudo-Voigt functions to account for peak asymmetry and extract integrated intensities. (e) Extracted ferroelectric domain volume fractions as a function of E. (f) Calculated effective k as a function of E. (g) "Achievable" k range when E is applied along the [001] direction and "Not demonstrated" when E is applied along the [100] or [010] direction.

ferroelectric SSTCDs — including thermal switches, diodes, and rectifiers — BTO achieves an exceptional SR due to its tetragonal crystal structure, where a pronounced difference between a- and c-domain thermal transport enables strong modulation of k under an applied E. First-principles calculations and in situ XRD confirm that E-driven redistribution of these domains governs the observed thermal tunability. Beyond performance, the ferroelectric thermal transistor offers several intrinsic advantages over conventional heat pumps: (i) ultralow power density on the order of μW cm^{-2}, compared with hundreds of μW cm^{-2} for typical vapor-compression-based heat pump systems; (ii) absence of moving parts; (iii) macroscopic dimensions with substantial

15214095, 0, Downloaded from https://advanced.onlinelibrary.wiley.com/doi/10.1002/adma.75838 by CochraneChina, Wiley Online Library on [27/11/2026]. See the Terms and Conditions (https://onlinelibrary.wiley.com/terms-and-conditions) on Wiley Online Library for rules of use; OA articles are governed by the applicable Creative Commons License

heat-carrying capacity; and (iv) compatibility with practical infrastructure-scale integration. Together, these results establish electrically gated ferroelectric materials as scalable platforms for programmable heat flow and provide a new perspective on utilizing a long-studied material system for energy-efficient thermal management.

Author Contributions

Conceptualization: GP, by, SH. data Curation: GP, BY, YM, SL, JK. Formal Analysis: GP, BY, YM. Funding Acquisition: SH. investigation: GP, BY, YM, JL, YS, SC. methodology: GP. project administration: SH. Resources: WK, HYL. Software: KK, HY, MC, SK. Supervision: JMB, HYL, THK, HJ, SK, SH. Validation: THK, HJ, SK, SH. Visualization: GP, SMS. Writing – original draft: GP. Writing – review & editing: GP, BY, YM, SH

Acknowledgements

The authors have nothing to report.

Funding

This work was supported by Samsung Research Funding Center of Samsung Electronics Under Project Number SRFC-MA2402-07, the National Research Foundation of Korea (NRF) grant funded by the Korean government (MSIT) (RS-2025-25463997, RS-2025-00558200, and RS-2026-25508298), computational resources from KISTI Supercomputing Center through KSC-2024-CRE-0357, and the Korea Institute of Science and Technology (26E0181, 26Z9052).

Conflicts of Interest

The authors declare no conflicts of interest.

Data Availability Statement

The data that support the findings of this study are available from the corresponding author upon reasonable request.

References

1. I. Staffell, S. Pfenninger, and N. Johnson, "A Global Model of Hourly Space Heating and Cooling Demand at Multiple Spatial Scales," *Nature Energy* 8 (2023): 1328–1344, https://doi.org/10.1038/s41560-023-01341-5.

2. L. E. Bell, "Cooling, Heating, Generating Power, and Recovering Waste Heat With Thermoelectric Systems," *Science* 321 (2008): 1457–1461, https://doi.org/10.1126/science.1158899.

3. S. Baldwin, Quadrennial Technology Review: An Assessment of Energy Technologies and Research Opportunities (2015).

4. "The Future of Cooling—Analysis", IEA (2018), 23, accessed: February 6, 2026, https://www.iea.org/reports/the-future-of-cooling.

5. S. Chu and A. Majumdar, "Opportunities and Challenges for a Sustainable Energy Future," *Nature* 488 (2012): 294–303, https://doi.org/10.1038/nature11475.

6. M. Li, H. Wu, E. M. Avery, et al., "Electrically Gated Molecular Thermal Switch," *Science* 382 (2023): 585–589, https://doi.org/10.1126/science.abo4297.

7. T. Swoboda, K. Klinar, A. S. Yalamarthy, A. Kitanovski, and M. M. Rojo, "Solid-State Thermal Control Devices," *Advanced Electronic Materials* 7 (2021): 2000625, https://doi.org/10.1002/aelm.202000625.

8. Y. Li, W. Li, T. Han, et al., "Transforming Heat Transfer With Thermal Metamaterials and Devices," *Nature Reviews Materials* 6 (2021): 488–507, https://doi.org/10.1038/s41578-021-00283-2.

9. C. Liu, C. Wu, Y. Zhao, et al., "Actively and Reversibly Controlling Thermal Conductivity in Solid Materials," *Physics Reports* 1058 (2024): 1–32, https://doi.org/10.1016/j.physrep.2024.01.001.

10. J. Jia, S. Li, X. Chen, and Y. Shigesato, "Emerging Solid–State Thermal Switching Materials," *Advanced Functional Materials* 34 (2024): 2406667, https://doi.org/10.1002/adfm.202406667.

11. M. Y. Wong, C. Y. Tso, T. C. Ho, and H. H. Lee, "A Review of State of the Art Thermal Diodes and Their Potential Applications," *International Journal of Heat and Mass Transfer* 164 (2021): 120607, https://doi.org/10.1016/j.ijheatmasstransfer.2020.120607.

12. Z. Chen, A. Li, W. Luo, P. Zhu, G. Zhu, and Y. Zeng, "A Review of Thermal Switches and Diodes for Energy and Information Technologies," *Thermo-X* 2 (2026): 202514–202514, https://doi.org/10.70401/tx.2026.0010.

13. G. Wehmeyer, T. Yabuki, C. Monachon, J. Wu, and C. Dames, "Thermal Diodes, Regulators, and Switches: Physical Mechanisms and Potential Applications," *Applied Physics Reviews* 4 (2017): 041304, https://doi.org/10.1063/1.5001072.

14. X. Moya and N. D. Mathur, "Caloric Materials for Cooling and Heating," *Science* 370 (2020): 797–803, https://doi.org/10.1126/science.abb0973.

15. A. Kitanovski, K. Klinar, E. Luo, et al., "Emerging Opportunities for High-Temperature Solid-State and Gas-Cycle Heat Pumps," *Nature Energy* 10 (2025): 1412–1426, https://doi.org/10.1038/s41560-025-01908-4.

16. A. Torelló, P. Lheritier, T. Usui, et al., "Giant Temperature Span in Electrocaloric Regenerator," *Science* 370 (2020): 125–129, https://doi.org/10.1126/science.abb8045.

17. J. Li, A. Torelló, V. Kovacova, et al., "High Cooling Performance in a Double-Loop Electrocaloric Heat Pump," *Science* 382 (2023): 801–805, https://doi.org/10.1126/science.adi5477.

18. B. Li, Y. Kawakita, S. Ohira-Kawamura, et al., "Colossal Barocaloric Effects in Plastic Crystals," *Nature* 567 (2019): 506–510, https://doi.org/10.1038/s41586-019-1042-5.

19. P. Lloveras, A. Aznar, M. Barrio, et al., "Colossal Barocaloric Effects near Room Temperature in Plastic Crystals of Neopentylglycol," *Nature Communications* 10 (2019): 1803, https://doi.org/10.1038/s41467-019-09730-9.

20. Y. D. Wang, S. J. Smullin, M. J. Sheridan, Q. Wang, C. Eldershaw, and D. E. Schwartz, "A Heat-Switch-Based Electrocaloric Cooler," *Applied Physics Letters* 107 (2015): 134103, https://doi.org/10.1063/1.4932164.

21. H. He, X. Niu, Z. Xu, et al., "Interdigitated Structure-Derived Scalable All-Solid-State Electrocaloric Cooling Device Using Lead-Free $BaSrTiO_3$-Based Multilayer Ceramics," *Joule* 9 (2025): 102128, https://doi.org/10.1016/j.joule.2025.102128.

22. J. F. Ihlefeld, B. M. Foley, D. A. Scrymgeour, et al., "Room-Temperature Voltage Tunable Phonon Thermal Conductivity via Reconfigurable Interfaces in Ferroelectric Thin Films," *Nano Letters* 15 (2015): 1791–1795, https://doi.org/10.1021/nl504505t.

23. Y. Lin, Y. Bao, S. Yan, et al., "Ferroelectric Polarization Modulated Thermal Conductivity in Barium Titanate Ceramic," *ACS Applied Materials & Interfaces* 14 (2022): 49928–49936, https://doi.org/10.1021/acsami.2c12388.

24. A. Negi, A. Rodriguez, X. Zhang, et al., "Thickness-Dependent Thermal Conductivity and Phonon Mean Free Path Distribution in Single-Crystalline Barium Titanate," *Advanced Science* 10 (2023): 2301273, https://doi.org/10.1002/advs.202301273.

25. L. Féger, C. Escorihuela-Sayalero, J.-M. Rampnoux, et al., "Lead-Free Room-Temperature Ferroelectric Thermal Conductivity Switch Using Anisotropies in Thermal Conductivities," *Physical Review Materials* 8 (2024): 094403, https://doi.org/10.1103/PhysRevMaterials.8.094403.

26. F. Zhang, G. Rui, Y. Quan, et al., "Electric-Field-Dependent Thermal Conductivity in Fresh and Aged Bulk Single Crystalline $BaTiO_3$," *Materials Science* 38 (2025): 5539–5549, https://doi.org/10.48550/arXiv.2511.14974.

15214095, 0, Downloaded from https://advanced.onlinelibrary.wiley.com/doi/10.1002/adma.75838 by CochraneChina, Wiley Online Library on [27/11/2026]. See the Terms and Conditions (https://onlinelibrary.wiley.com/terms-and-conditions) on Wiley Online Library for rules of use; OA articles are governed by the applicable Creative Commons License

27. E. Langenberg, D. Saha, M. E. Holtz, et al., "Ferroelectric Domain Walls in $PbTiO_3$ Are Effective Regulators of Heat Flow at Room Temperature," *Nano Letters* 19 (2019): 7901–7907, https://doi.org/10.1021/acs.nanolett.9b02991.

28. J. A. Seijas-Bellido, J. Íñiguez, and R. Rurali, "Anisotropy-Driven Thermal Conductivity Switching and Thermal Hysteresis in a Ferroelectric," *Applied Physics Letters* 115 (2019): 192903, https://doi.org/10.1063/1.5127825.

29. C. Liu, Y. Chen, and C. Dames, "Electric-Field-Controlled Thermal Switch in Ferroelectric Materials Using First-Principles Calculations and Domain-Wall Engineering," *Physical Review Applied* 11 (2019): 044002, https://doi.org/10.1103/PhysRevApplied.11.044002.

30. C. Liu, Z. Chen, C. Wu, et al., "Large Thermal Conductivity Switching in Ferroelectrics by Electric Field-Triggered Crystal Symmetry Engineering," *ACS Applied Materials & Interfaces* 14 (2022): 46716–46725, https://doi.org/10.1021/acsami.2c11530.

31. B. M. Foley, M. Wallace, J. T. Gaskins, et al., "Voltage-Controlled Bistable Thermal Conductivity in Suspended Ferroelectric Thin-Film Membranes," *ACS Applied Materials & Interfaces* 10 (2018): 25493–25501, https://doi.org/10.1021/acsami.8b04169.

32. B. L. Wooten, R. Iguchi, P. Tang, et al., "Electric Field–Dependent Phonon Spectrum and Heat Conduction in Ferroelectrics," *Science Advances* 9 (2023): add7194, https://doi.org/10.1126/sciadv.add7194.

33. S. Ning, S. C. Huberman, C. Zhang, Z. Zhang, G. Chen, and C. A. Ross, "Dependence of the Thermal Conductivity of $BiFeO_3$ Thin Films on Polarization and Structure," *Physical Review Applied* 8 (2017): 054049, https://doi.org/10.1103/PhysRevApplied.8.054049.

34. S. Deng, J. Yuan, Y. Lin, et al., "Electric-Field-Induced Modulation of Thermal Conductivity in Poly(vinylidene fluoride)," *Nano Energy* 82 (2021): 105749, https://doi.org/10.1016/j.nanoen.2021.105749.

35. C. Liu, Y. Si, H. Zhang, et al., "Low Voltage–Driven High-Performance Thermal Switching in Antiferroelectric PbZrO 3 Thin Films," *Science* 382 (2023): 1265–1269, https://doi.org/10.1126/science.adj9669.

36. K. Aryana, J. A. Tomko, R. Gao, et al., "Observation of Solid-State Bidirectional Thermal Conductivity Switching in Antiferroelectric Lead Zirconate ($PbZrO_3$) ($PbZrO_3$)," *Nature Communications* 13 (2022): 1573, https://doi.org/10.1038/s41467-022-29023-y.

37. G. Park, B. Yoon, J. Lee, et al., "Low-Voltage Driven Ferroelectric Thermal Switch," *Nano Energy* 145 (2025): 111410, https://doi.org/10.1016/j.nanoen.2025.111410.

38. A. Negi, H. P. Kim, Z. Hua, et al., "Ferroelectric Domain Wall Engineering Enables Thermal Modulation in PMN–PT Single Crystals," *Advanced Materials* 35 (2023): 2211286, https://doi.org/10.1002/adma.202211286.

39. P. Upreti, D. Rashadfar, R. Sahul, et al., "Electric Field Control of Phonon Lifetimes and Thermal Conductivity in Relaxor-Based Ferroelectric," *PRX Energy* 5 (2026): 013001, https://doi.org/10.1103/5d1z-wg4p.

40. D. Rashadfar, B. L. Wooten, and J. P. Heremans, "Electric Field-Dependent Thermal Conductivity of Relaxor Ferroelectric PMN-33PT Through Changes in the Phonon Spectrum," *Materials Horizons* 12 (2025): 3341–3348, https://doi.org/10.1039/D4MH01845A.

41. D. Barneo, M. Royo, R. Ramos, et al., "The Coupling of Ferroelectric Polarization and Oxygen Vacancy Migration Enables Electrically Controlled Thermal Memories," *Advanced Materials* 38 (2026): 19670, https://doi.org/10.1002/adma.202519670.

42. C. Liu, V. Mishra, Y. Chen, and C. Dames, "Large Thermal Conductivity Switch Ratio in Barium Titanate Under Electric Field Through First-Principles Calculation," *Advanced Theory and Simulations* 1 (2018): 1800098, https://doi.org/10.1002/adts.201800098.

43. J. Zhang, C. Bin, Y. Zhao, et al., "Quantification of Switchable Thermal Conductivity of Ferroelectric Materials Through Second-Principles Calculation," *Materials Today Physics* 41 (2024): 101347, https://doi.org/10.1016/j.mtphys.2024.101347.

44. A. K. Das, P. Mishra, S. S. Biswal, A. Tripathy, and S. Bhuyan, "*Processing and Development of Lead Free Bi*($Ni_{2/3}Nb_{1/3}$)O_3 Ferroelectric Material for Thermal Sensing Electronic Device," *Transactions on Electrical and Electronic Materials* 27 (2026), 156–164, https://doi.org/10.1007/s42341-025-00646-4.

45. V. Shekar and M. Krarti, "Control Strategies for Dynamic Insulation Materials Applied to Commercial Buildings," *Energy and Buildings* 154 (2017): 305–320, https://doi.org/10.1016/j.enbuild.2017.08.084.

46. Q. Lu, S. Huberman, H. Zhang, et al., "Bi-Directional Tuning of Thermal Transport in $SrCoO_x$ With Electrochemically Induced Phase Transitions," *Nature Materials* 19 (2020): 655–662, https://doi.org/10.1038/s41563-020-0612-0.

47. Q. Yang, J. Lee, H. Jeen, H. J. Cho, and H. Ohta, "Solid-State Electrochemical Protonation of $SrCoO_{2.5}$ Into $H_xSrCoO_{2.5}$ (x = 1, 1.5, and 2)," *ACS Applied Electronic Materials* 3 (2021): 3296–3300, https://doi.org/10.1021/acsaelm.1c00505.

48. Y. Zhang, W. M. Postiglione, R. Xie, et al., "Wide-range Continuous Tuning of the Thermal Conductivity of $La_{0.5}Sr_{0.5}CoO_{3-\delta}$ Films via Room-temperature Ion-gel Gating," *Nature Communications* 14 (2023): 2626, https://doi.org/10.1038/s41467-023-38312-z.

49. "The Future of Heat Pumps—Analysis", IEA (2022), 25–32, accessed February 13, 2026, https://www.iea.org/reports/the-future-of-heat-pumps.

50. P. Li, J. Zhang, J. Luo, et al., "Polarization Characteristics and Electric Domain Evolution of Ferroelectric and Antiferroelectric Materials," *Physica B: Condensed Matter* 724 (2026): 418163, https://doi.org/10.1016/j.physb.2025.418163.

51. Z. Ghemari and S. Belkhiri, "Exploring Novel Piezoelectric Materials With Enhanced Thermal Stability for High-Performance Sensors," *Transactions on Electrical and Electronic Materials* 26 (2025): 289–304, https://doi.org/10.1007/s42341-025-00600-4.

52. M. Tachibana, T. Kolodiazhnyi, and E. Takayama-Muromachi, "Thermal Conductivity of Perovskite Ferroelectrics," *Applied Physics Letters* 93 (2008): 092902, https://doi.org/10.1063/1.2978072.

53. Đ. Dangić, O. Hellman, S. Fahy, and I. Savić, "The Origin of the Lattice Thermal Conductivity Enhancement at the Ferroelectric Phase Transition in GeTe," *npj Computational Materials* 7 (2021): 57, https://doi.org/10.1038/s41524-021-00523-7.

54. M. A. Weilert, M. E. Msall, A. C. Anderson, and J. P. Wolfe, "Phonon Scattering From Ferroelectric Domain Walls: Phonon Imaging in KDP," *Physical Review Letters* 71 (1993): 735–738, https://doi.org/10.1103/PhysRevLett.71.735.

55. D. Vanderbilt and K. M. Rabe, "First-Principles Theory of Ferroelectric Phase Transitions for Perovskites: The Case of $BaTiO_3$," *Physical Review B* 52 (1995): 6301–6312, https://doi.org/10.1103/PhysRevB.52.6301.

56. "Pyroelectricity in Ferroelectric $PbTiO_3$ Enhanced by A-Site Cation Contribution and Negative Thermal Expansion," *Journal of Physical Chemistry C* 128 (2024): 16199–16207, https://doi.org/10.1021/acs.jpcc.4c04514.

57. K. Eklund and A. J. Karttunen, "Pyroelectric Effect in Tetragonal Ferroelectrics $BaTiO_3$ and $KNbO_3$ Studied With Density Functional Theory," *Journal of Physical Chemistry C* 127 (2023): 21806–21815, https://doi.org/10.1021/acs.jpcc.3c05513.

58. D. Balzar, "Voight Function Model in Diffraction-Line Broadening Analysis," *NIST Chap.* 7 (1999), https://www.nist.gov/publications/voight-function-model-diffraction-line-broadening-analysis.

59. B. Li, M. C. Ehmke, J. E. Blendell, and K. J. Bowman, "Optimizing Electrical Poling for Tetragonal, Lead-Free BZT–BCT Piezoceramic Alloys," *Journal of the European Ceramic Society* 33 (2013): 3037–3044, https://doi.org/10.1016/j.jeurceramsoc.2013.05.032.

15214095, 0, Downloaded from https://advanced.onlinelibrary.wiley.com/doi/10.1002/adma.75838 by CochraneChina, Wiley Online Library on [27/11/2026]. See the Terms and Conditions (https://onlinelibrary.wiley.com/terms-and-conditions) on Wiley Online Library for rules of use; OA articles are governed by the applicable Creative Commons License

60. R. Jayavel, S. Madeswaran, R. M. Kumar, K. Terabe, and K. Kitamura, "Domain Patterns on Ferroelectric Rh:$BaTiO_3$ Single Crystals," *Materials Science and Engineering: B* 120 (2005): 137–140, https://doi.org/10.1016/j.mseb.2005.02.040.

Supporting Information

Additional supporting information can be found online in the Supporting Information section.

Supporting File 1: adma75838-sup-0001-SuppMat.docx.

Supporting File 2: adma75838-sup-0002-MovieS1.mp4.

Supporting File 3: adma75838-sup-0003-MovieS2.mp4.

15214095, 0, Downloaded from https://advanced.onlinelibrary.wiley.com/doi/10.1002/adma.75838 by CochraneChina, Wiley Online Library on [27/11/2026]. See the Terms and Conditions (https://onlinelibrary.wiley.com/terms-and-conditions) on Wiley Online Library for rules of use; OA articles are governed by the applicable Creative Commons License